ARCHIVES OF MECHANICS
Arch. Mech. **77** (∗), ∗∗∗–∗∗∗, 2025, DOI: 10.24423/aom.4640

Mean-field/FMBEM homogenization of 3-D particulate composites

J. PTASZNY

Department of Computational Mechanics and Engineering,
Silesian University of Technology, ul. Konarskiego 18a, 44-100 Gliwice, Poland
e-mail: jacek.ptaszny@polsl.pl

An approach to homogenization of particulate composite materials is proposed. The mean-field assumption for averaging over phases is combined with numerical calculations of strain-concentration tensors, thus making it independent from the analytical Eshelby solution for ellipsoidal inclusions. The fast multipole boundary element method (FMBEM) is applied to 3-D elasticity and two-phase composites. As opposed to the finite element method (FEM), this method allows for easy modeling of large structures without the need to discretize volumes. Single-inhomogeneity problems are solved, and the calculated strain concentration tensors are used in the averaging formula under the assumption of the Mori–Tanaka approach. An interpolative scheme involving the inverse Mori–Tanaka assumption, known from the literature, is also applied to increase the accuracy of the approximation for higher volume fractions of particles. Examples include composites with spherical and cubic particles, and hybrid materials with auxetic components. The results are consistent with analytical solutions and RVE/FEM models.

Key words: 3-D particulate composites, linear elasticity, mean-field homogenization, strain concentration tensor, fast multipole boundary element method.

1. Introduction

Mean-field homogenization is a group of methods for determining the effective properties of inhomogeneous materials. It includes the Mori–Tanaka method that involves the analytical Eshelby solution for the ellipsoidal inclusion problem in linear elasticity [1–9]. The approach can model such shapes of inhomogeneities as short or long fibers, platelets, spheres, or spheroids. Although the Mori–Tanaka approach does not take into account the direct interaction between inhomogeneities, it is still considered efficient due to its low computational cost.

The scope of applications of analytical mean-field approaches can be extended by incorporating numerical methods to calculate the strain contribution of a single inhomogeneity. For example, in [10], 3-D finite element models of polymer composites reinforced with wavy nanotubes were analyzed to compute

the numerical strain concentration tensor of the reinforcement. The tensor was combined with the Mori–Tanaka approach to achieve the effective elastic moduli of the composite. The paper [11] considers the mean-field (Mori–Tanaka) homogenization approach coupled with the finite element method (FEM) for 3-D problems with elastoplastic matrix and ellipsoidal inhomogeneities. The FEM models were used to compute average strains over inhomogeneity in the equivalent inclusion problem. Macroscopic stress-strain relations of the composites were determined. In the work [12], the FEM was applied to 3-D models with single inclusion with various shapes: prolate spheroidal, oblate spheroidal, cylindrical, triangular prism, rectangular prism and irregular prism. The strain concentration tensor calculated numerically was applied to determine the effective properties of composites with aligned and randomly oriented inhomogeneities. The Mori–Tanaka approach combined with the FEM was applied in [13] to establish an incremental method for the analysis of 3-D elastoplastic composites. In [14], 3-D FEM models of single-inclusion problems with spherical and cubic particles were analysed and used to calculate effective elastic constants of composites within the linear elastic regime, and stress-strain relationships for inelastic composites. The work was continued in [15] to establish a two-stage homogenization method involving the pseudograin discretization method. The properties of inelastic short-fiber reinforced composites were analyzed. Recently, the approach has been applied to construct a data-driven time-efficient model to homogenize nonlinear short fiber composites [16]. Another efficient analytical-numerical approach to model composites with arbitrary shapes of inhomogeneities is the calculation of compliance or stiffness contribution tensors, which relate uniform stress or strain boundary conditions to extra strains or stresses caused by a single inhomogeneity. The change in overall compliance or stiffness of the composite depends on the contribution tensors and the volume fraction of the inhomogeneities [17]. The approach was coupled with the FEM [18] and a meshless method [19] and applied to 2D and 3D composites.

The combination of the above approaches with the FEM requires a numerical solution of the single-inhomogeneity problem, i.e., a solid body or prism (usually a cube) containing a single inhomogeneity. As the model approximates an infinite medium with single inhomogeneity for the dilute strain concentration tensor, the inhomogeneity must be small enough compared to the whole model to diminish the effect of the external boundary. Thus, in the FEM, the coarse mesh on the external boundary of the model must be connected with the fine mesh of the inhomogeneity. This results in the excessive size of the discretized problem even for a simple geometry of the inhomogeneity. Therefore, a possible method for the reduction of the problem and simplification of the pre- and post-processing stages at once is the boundary element method (BEM). In the literature, papers containing results of self-consistent and Mori–Tanaka approaches combined with

the BEM for 2-D piezoelectric materials with elliptic voids [20] and circular inhomogeneities [21] are available. Similarly, papers [22, 23] and monograph [24] contain results of the Mori–Tanaka approach applications for 2-D piezoelectric composites with circular inhomogeneities. To the best of our knowledge, there are no other publications available in the literature concerning the coupling of the BEM with the mean-field homogenization approach for different types of nonhomogeneous materials. The advantageous feature of the BEM of discretizing only the boundary is more relevant for 3-D problems than for 2-D ones. This fact was the motivation for further investigation of this topic.

The present contribution aims to combine the fast multipole boundary element method (FMBEM) [25], for 3-D linear elasticity with the formulation for inhomogeneities and mean-field homogenization approach. For the considered class of problems, the method requires only the discretization of the boundary. The FMBEM is placed among novel versions of the BEM, that has a computational complexity of type $O(N)$ or $O(N \log N)$, as opposed to the conventional BEM with at least $O(N^2)$ complexity, where N stands for the number of degrees of freedom of the discretized structure. The new approach is applied to composites reinforced with particles. The mean-field formulations include the Mori–Tanaka approach and the interpolative scheme with the inverse Mori–Tanaka method [26]. The considered materials include composites with spherical particles, for which analytical solutions are available and applied here to the validation of the proposed approach, composites with randomly distributed and oriented cubic particles (validated with literature results obtained by the mean-field/FEM approach and full FEM models of representative volume elements, RVEs) and hybrid materials with aligned auxetic subregions (also validated by RVE/FEM models). The last case illustrates how the space of elastic properties of new materials can be efficiently explored for their optimal stiffness. According to the literature, the effective Young modulus has a local minimum for a certain value of the volume fraction of the auxetic phase [27, 28]. The whole investigation illustrates the capability of the mean-field/FMBEM approach to minimize the number of the boundary value problems to be solved for the inhomogeneity strain concentration tensor, minimize the size and solution time of the discretized boundary value problems compared to RVE/FEM models, and make the preprocessing stage extremely easy and robust.

The paper is organized as follows: the second section introduces the mean-field approach coupled with the numerical calculation of the inhomogeneity strain concentration tensor. Section 3 contains a description of the basic equations applied and solved in the boundary element method. It also contains the most important information on the fast multipole BEM (FMBEM). Section 4 contains three numerical examples. The first example concerns composite materials with spherical particles. The second example is a composite material reinforced

with randomly distributed and oriented cubic particles. The third example illustrates the exploration of the space of elastic properties for a new hybrid material. Furthermore, Section 4 compares averaged strains in phases of selected materials computed by different methods. The last section contains conclusions. The paper is supplemented with Appendix with the Mori–Tanaka mean-field/FMBEM predictions of elastic moduli of the hybrid materials that were less accurate than the interpolative scheme.

2. Hybrid mean-field/numerical homogenization

Consider an analysis of a structure in the macro scale. For a given point, the macro strain $\bar{\varepsilon}$ is known and macro stresses $\bar{\sigma}$ are to be found, or the opposite situation is considered. For linear elasticity, the macro strain and stress are related by the overall macro stiffness tensor $\bar{\boldsymbol{C}}$ (bold italic symbols denote the 4th-order tensors):

$$\bar{\boldsymbol{\sigma}} = \bar{\boldsymbol{C}} : \bar{\boldsymbol{\varepsilon}} \quad \text{or} \quad \bar{\sigma}_{ij} = \bar{C}_{ijkl}\bar{\varepsilon}_{kl}. \tag{2.1}$$

At the micro-level, the point corresponds to a representative volume element (RVE) with the domain Ω. The macro strain and stresses correspond to respective quantities, averaged over Ω:

$$\langle \varepsilon \rangle = \bar{\boldsymbol{\varepsilon}}, \qquad \langle \sigma \rangle = \bar{\boldsymbol{\sigma}}, \quad \langle f \rangle = \frac{1}{V}\int\limits_{\Omega} f \,\mathrm{d}V, \tag{2.2}$$

where V is the RVE volume. For a two-phase composite, the average can be expressed by using averages over constituents: matrix Ω_0 and inhomogeneity Ω_1, and their volume fractions c_0, c_1:

$$\langle f \rangle = c_0 \langle f \rangle_{\Omega_0} + c_1 \langle f \rangle_{\Omega_1} = (1 - c_1) \langle f \rangle_{\Omega_0} + c_1 \langle f \rangle_{\Omega_1} . \tag{2.3}$$

On the RVE boundary, linear displacement boundary conditions are imposed, corresponding to $\bar{\boldsymbol{\varepsilon}}$. Strain averages in phases are related to the macro strain by strain concentration tensors, the local one $\boldsymbol{B}$ (e.g. [7, 8]):

$$\langle \varepsilon \rangle_{\Omega_1} = \boldsymbol{B} : \langle \varepsilon \rangle_{\Omega_0} , \tag{2.4}$$

and the global one $\boldsymbol{A}$:

$$\langle \boldsymbol{\varepsilon} \rangle_{\Omega_1} = \boldsymbol{A} : \bar{\varepsilon}, \quad \boldsymbol{A} = \boldsymbol{B} : [(1 - c_1)\boldsymbol{I} + c_1 \boldsymbol{B}]^{-1} , \tag{2.5}$$

where $\boldsymbol{I}$ is the fourth-order identity tensor. The macro stiffness tensor is then expressed as:

$$\begin{aligned} \bar{\boldsymbol{C}} &= \boldsymbol{C}_0 + c_1(\boldsymbol{C}_1 - \boldsymbol{C}_0) : \boldsymbol{A} \\ &= \boldsymbol{C}_0 + c_1(\boldsymbol{C}_1 - \boldsymbol{C}_0) : \boldsymbol{B} : [(1 - c_1)\boldsymbol{I} + c_1 \boldsymbol{B}]^{-1}. \end{aligned} \tag{2.6}$$

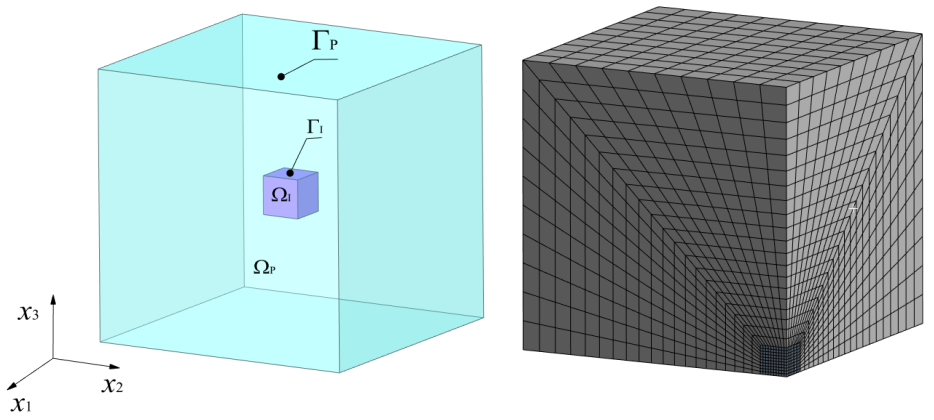

(a) (b)

FIG. 1. The single-inhomogeneity problem: a) geometry, b) typical FEM model analysed in the literature (one eight of the model with symmetry conditions on appropriate external faces) [14].

For the Mori–Tanaka assumption, the strain concentration tensor comes from the solution of the single-inhomogeneity problem. The original Mori–Tanaka model employs the Eshelby solution to compute the strain concentration tensor. Thus, such an approach is limited to ellipsoidal inclusions. On the other hand, to handle non-ellipsoidal shapes, the problem can be solved by using numerical methods, e.g., FEM or BEM, and the strain concentration tensors can be calculated numerically. A single inhomogeneity with properties $\boldsymbol{C}_0$ is embedded within a prism Ω_P with external boundary Γ_P (Fig. 1a). The prism has material properties of the matrix ($\boldsymbol{C}_0$) and approximates an infinite medium with far-field (macro) strain imposed on its boundary:

$$u_i|_{\Gamma_\mathrm{P}} = \tilde{\varepsilon}_{ij}^{I-VI} \cdot x_j, \tag{2.7}$$

$$\tilde{\varepsilon}_{ij}^{I-VI} = \begin{bmatrix} 1 & 0 & 0 \\ 0 & 0 & 0 \\ 0 & 0 & 0 \end{bmatrix}, \begin{bmatrix} 0 & 0 & 0 \\ 0 & 1 & 0 \\ 0 & 0 & 0 \end{bmatrix}, \begin{bmatrix} 0 & 0 & 0 \\ 0 & 0 & 0 \\ 0 & 0 & 1 \end{bmatrix}, \begin{bmatrix} 0 & 0 & 0 \\ 0 & 0 & 1 \\ 0 & 1 & 0 \end{bmatrix}, \begin{bmatrix} 0 & 0 & 1 \\ 0 & 0 & 0 \\ 1 & 0 & 0 \end{bmatrix}, \begin{bmatrix} 0 & 1 & 0 \\ 1 & 0 & 0 \\ 0 & 0 & 0 \end{bmatrix}. \tag{2.8}$$

The average strain over the inhomogeneity Ω_I with the boundary Γ_I (which is also the matrix-inhomogeneity interface) is calculated by the volume integral applicable in the case of the FEM (Fig. 1b):

$$\langle \varepsilon_{ij} \rangle_{\Omega_\mathrm{I}} = \frac{1}{V_\mathrm{I}} \int_{\Omega_\mathrm{I}} \varepsilon_{ij} \, \mathrm{d}\Omega_\mathrm{I}, \tag{2.9}$$

with V_I being the volume of the inhomogeneity. Note that for a boundary method, the natural way for the calculation of average strain is rather calculation of the surface integral over the inhomogeneity boundary [20–22]:

$$\langle \varepsilon_{ij} \rangle_{\Omega_\mathrm{I}} = \frac{1}{2V_\mathrm{I}} \int\limits_{\Gamma_\mathrm{I}} (u_i n_j + u_j n_i)\, \mathrm{d}\Gamma_\mathrm{I}. \tag{2.10}$$

For the numerical determination of the dilute (local) strain concentration tensor, one can follow the procedure proposed in [10]. Assume that the matrix is large enough to appear infinite to the inclusion and there is a linear relationship between the far-field strain tensor $\tilde{\varepsilon}^p_{ij}$ and the average strain in inclusion $\langle \boldsymbol{\varepsilon} \rangle_{\Omega_1}$. The relationship involves the local strain concentration tensor:

$$\langle \boldsymbol{\varepsilon} \rangle_{\Omega_1} = \boldsymbol{B} : \tilde{\boldsymbol{\varepsilon}}^p. \tag{2.11}$$

It is convenient to present the relationship in the matrix form:

$$\begin{Bmatrix} \langle \varepsilon_{11} \rangle_{\Omega_1} \\ \langle \varepsilon_{22} \rangle_{\Omega_1} \\ \langle \varepsilon_{33} \rangle_{\Omega_1} \\ \langle \varepsilon_{23} \rangle_{\Omega_1} \\ \langle \varepsilon_{13} \rangle_{\Omega_1} \\ \langle \varepsilon_{12} \rangle_{\Omega_1} \end{Bmatrix} = \begin{bmatrix} B_{11} & B_{12} & B_{13} & B_{14} & B_{15} & B_{16} \\ B_{21} & B_{22} & B_{23} & B_{24} & B_{25} & B_{26} \\ B_{31} & B_{32} & B_{33} & B_{34} & B_{35} & B_{36} \\ B_{41} & B_{42} & B_{43} & B_{44} & B_{45} & B_{46} \\ B_{51} & B_{52} & B_{53} & B_{54} & B_{55} & B_{56} \\ B_{61} & B_{62} & B_{63} & B_{64} & B_{65} & B_{66} \end{bmatrix} \begin{Bmatrix} \tilde{\varepsilon}^p_{11} \\ \tilde{\varepsilon}^p_{22} \\ \tilde{\varepsilon}^p_{33} \\ \tilde{\varepsilon}^p_{23} \\ \tilde{\varepsilon}^p_{13} \\ \tilde{\varepsilon}^p_{12} \end{Bmatrix}, \tag{2.12}$$

where columns of the matrix B_{ip} $(i, p = 1, 2, \ldots, 6)$ are calculated by averaging of strains caused by the far-field strain tests I–VI:

$$B_{ip} = \frac{\langle \varepsilon_i \rangle_{\Omega_1} |_{\tilde{\varepsilon}^p}}{\tilde{\varepsilon}^p_i}, \qquad \tilde{\varepsilon}^p \in \{\tilde{\varepsilon}^{I-VI}\}. \tag{2.13}$$

Thus, in the general case of non-symmetric inhomogeneities, elements of the dilute strain concentration tensor $\boldsymbol{B}$ and macro stiffness tensor $\bar{\boldsymbol{C}}$ are calculated by performing 6 tests.

For misaligned inhomogeneities, one can reconsider Eq. (2.6) to express the effective stiffness by terms that are orientation independent and orientation dependent [29]:

$$\bar{\boldsymbol{C}} = \boldsymbol{C}_0 + \{\boldsymbol{C}\}. \tag{2.14}$$

The orientation dependent part can be calculated by the averaging formula:

$$\{C_{ijkl}\} = \int\limits_0^{2\pi} \int\limits_0^{2\pi} \int\limits_0^{\pi} g(\theta, \psi, \phi) \alpha_{ip} \alpha_{jq} \alpha_{kr} \alpha_{ls} C_{pqrs} \sin(\theta)\, \mathrm{d}\theta\, \mathrm{d}\psi\, \mathrm{d}\phi, \tag{2.15}$$

with $g(\theta, \psi, \phi)$ being the orientation distribution function equal to 1 for random orientation and dependent on Euler angles (θ, ψ, ϕ) in general case. Functions α_{ij} can be found, e.g., in [8, 29]. The averaging over orientations assures that the computed effective elastic stiffness is symmetric.

To improve the mean-field predictions for higher volume fractions of particles, one can apply the double inclusion model [6] combined with the interpolative scheme applied in [7, 26] that involves the calculations of two strain concentration tensors:

- $\boldsymbol{B}_l = \boldsymbol{B}(\boldsymbol{C}_0, \boldsymbol{C}_1)$ – the tensor of the Mori–Tanaka approach,
- $\boldsymbol{B}_u = \boldsymbol{B}(\boldsymbol{C}_1, \boldsymbol{C}_0)^{-1}$ – tensor of the inverse Mori–Tanaka model for which properties of the inclusions and matrix are permuted.

The interpolation model uses the combinantion of these tensors for the double-inclusion interpolative approach strain concentration tensor:

$$\boldsymbol{B}_{D-I} = \{[1 - \zeta(c_1)]\boldsymbol{B}_l^{-1} + \zeta(c_1)\boldsymbol{B}_u^{-1}\}^{-1}, \tag{2.16}$$

with the interpolation function:

$$\zeta(c_1) = \frac{1}{2}c_1(1 + c_1). \tag{2.17}$$

The approach requires the solution of additional six boundary value problems with permuted properties of the matrix and inhomogeneity for $\boldsymbol{B}_u$.

3. BEM solution of the single-inhomogeneity problem

3.1. Basic equations of the BEM

Consider a general problem of the homogeneous body Ω with the boundary Γ, that is made of isotropic material. The boundary integral equation takes the form [30–33, 36]:

$$C_{ij}(\mathbf{x}')u_j(\mathbf{x}') + \int_\Gamma T_{ij}(\mathbf{x}', \mathbf{x})u_j(\mathbf{x})\mathrm{d}\Gamma(\mathbf{x}) = \int_\Gamma U_{ij}(\mathbf{x}', \mathbf{x})t_j(\mathbf{x})\,\mathrm{d}\Gamma(\mathbf{x}), \tag{3.1}$$

where $\mathbf{x}$ and $\mathbf{x}'$ denote the collocation and integration point, C_{ij} $(i, j = 1, 2, 3)$ is a coefficient depending on the position of the collocation point and shape of the boundary at $\mathbf{x}'$, T_{ij} and U_{ij} are Kelvin fundamental solutions, u_i and t_i denote boundary displacements and traction forces. The fundamental solutions are defined by:

$$U_{ij}(\mathbf{x}', \mathbf{x}) = \frac{1}{16\pi\mu(1-\nu)r}[(3-4\nu)\delta_{ij} + r_{,i}\, r_{,j}\,], \tag{3.2}$$

$$T_{ij}(\mathbf{x}', \mathbf{x}) = -\frac{1}{8\pi(1-\nu)r^2} \times \left\{[(1-2\nu)\delta_{ij} + 3r_{,i}\, r_{,j}\,]\frac{\partial r}{\partial n} - (1-2\nu)(r_{,i}\, n_j - r_{,j}\, n_i)\right\}, \tag{3.3}$$

where μ is the shear modulus, ν – Poisson's ratio, δ_{ij} – the Kronecker symbol, n_j – component of the unit outward vector normal to the boundary, and r_i – component of vector connecting $\mathbf{x}'$ to $\mathbf{x}$.

The boundary of the body and the boundary quantities are discretized by using boundary elements. In this work, 8-node serendipity elements are applied (Fig. 2). Shape functions for these elements can be found elsewhere, e.g., in [33].

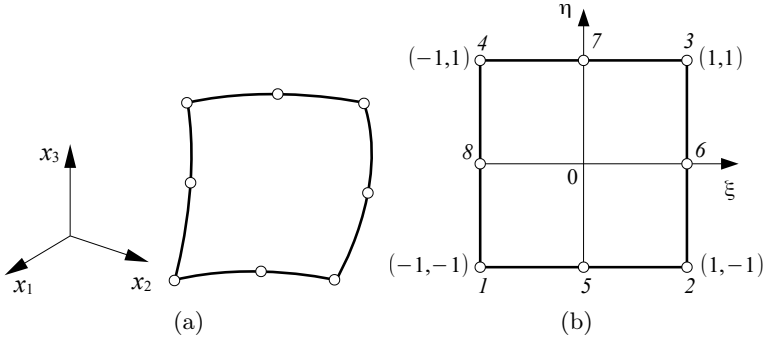

FIG. 2. 3D Serendipity boundary element with 8 nodes: a) in the global coordinate system x_i $(i = 1, 2, 3)$, b) in local coordinate system (ξ, η) for the numerical integration.

The discretization and application of (3.1) to all boundary nodes as $\mathbf{x}'$ leads to the formation of the matrix system of equations:

$$\mathbf{Hu} = \mathbf{Gt}, \tag{3.4}$$

where $\mathbf{G}$ and $\mathbf{H}$ are matrices dependent on the fundamental solutions, and $\mathbf{u}$ and $\mathbf{t}$ are vectors of boundary displacements and traction respectively. By taking into account boundary conditions and rearranging the system, it takes the form:

$$\mathbf{Ly} = \mathbf{Rz}, \tag{3.5}$$

where $\mathbf{y}$ and $\mathbf{z}$ denote vectors of unknown and known boundary quantities, respectively.

The numerical calculation of integrals in (3.1), which depend on singular fundamental solutions, requires the application of regularization techniques and

adaptive integration methods. We refer the Reader to [32, 33] for the detailed description of methods that can be applied for the present higher order discretization scheme.

3.2. Formulation for the single-inhomogeneity problem

In the case of the single-inhomogeneity problem (Fig. 1a), one can write the boundary integral equation for both phases separately, i.e., for the prism with the boundary $\Gamma_{\mathrm{P}} \cup \Gamma_{\mathrm{I}}$ [34]:

$$C_{ij}(\mathbf{x}')u_j(\mathbf{x}') + \int\limits_{\Gamma_{\mathrm{P}}\cup\Gamma_{\mathrm{I}}} T^{\mathrm{P}}_{ij}(\mathbf{x}',\mathbf{x})u_j(\mathbf{x})\,\mathrm{d}\Gamma(\mathbf{x}) = \int\limits_{\Gamma_{\mathrm{P}}\cup\Gamma_{\mathrm{I}}} U_{ij}(\mathbf{x}',\mathbf{x})t^{\mathrm{P}}_j(\mathbf{x})\,\mathrm{d}\Gamma(\mathbf{x}), \tag{3.6}$$

and the inhomogeneity with the boundary Γ_{I}:

$$C_{ij}(\mathbf{x}')u_j(\mathbf{x}') + \int\limits_{\Gamma_{\mathrm{I}}} T^{\mathrm{I}}_{ij}(\mathbf{x}',\mathbf{x})u_j(\mathbf{x})\,\mathrm{d}\Gamma(\mathbf{x}) = \int\limits_{\Gamma_{\mathrm{I}}} U_{ij}(\mathbf{x}',\mathbf{x})t^{\mathrm{I}}_j(\mathbf{x})\,\mathrm{d}\Gamma(\mathbf{x}). \tag{3.7}$$

Note that respective integrals over Γ_{I} involve actual direction of its outward unit normal vector which is opposite for the prism and inhomogeneity at given $\mathbf{x} \in \Gamma_{\mathrm{I}}$.

By taking into account the discretization and boundary conditions of the single-inhomogeneity problem, one can write the above equations as follows:

$$\begin{bmatrix} \mathbf{L}^{\mathrm{P}}_{11} & \mathbf{L}^{\mathrm{P}}_{12} \\ \mathbf{L}^{\mathrm{P}}_{21} & \mathbf{L}^{\mathrm{P}}_{22} \end{bmatrix} \begin{Bmatrix} \mathbf{t}^{\mathrm{P}} \\ \mathbf{u}^{\mathrm{PI}} \end{Bmatrix} = \begin{bmatrix} \mathbf{R}^{\mathrm{P}}_{11} & \mathbf{R}^{\mathrm{P}}_{12} \\ \mathbf{R}^{\mathrm{P}}_{21} & \mathbf{R}^{\mathrm{P}}_{22} \end{bmatrix} \begin{Bmatrix} \mathbf{u}^{\mathrm{P}} \\ \mathbf{t}^{\mathrm{PI}} \end{Bmatrix}, \tag{3.8}$$

$$\mathbf{H}^{\mathrm{I}}\mathbf{u}^{\mathrm{I}} = \mathbf{G}^{\mathrm{I}}\mathbf{t}^{\mathrm{I}}. \tag{3.9}$$

Vectors $\mathbf{t}^{\mathrm{P}}$ and $\mathbf{u}^{\mathrm{PI}}$ denote unknown tractions, on the outer boundary Γ_{P} of the prism, and displacements on the interface boundary Γ_{I}, respectively. Vectors $\mathbf{u}^{\mathrm{P}}$ and $\mathbf{t}^{\mathrm{PI}}$ denote known displacements on Γ_{P} and yet unknown tractions on the interface $\mathbf{t}^{\mathrm{PI}}$. Vectors $\mathbf{u}^{\mathrm{I}}$ and $\mathbf{t}^{\mathrm{I}}$ denote unknown displacements and tractions on the boundary of inhomogeneity Γ_{I}. Matrices $\mathbf{L}^{\mathrm{P}}_{ij}$, $\mathbf{R}^{\mathrm{P}}_{ij}$ $(i,j=1,2)$ depend on the terms of Eq. (3.6) built for the prism. Matrices $\mathbf{G}^{\mathrm{I}}$, $\mathbf{H}^{\mathrm{I}}$ are dependent on the terms of Eq. (3.7) built for the inhomogeneity.

Traction forces on the inhomogeneity boundary are:

$$\mathbf{t}^{\mathrm{I}} = (\mathbf{G}^{\mathrm{I}})^{-1}\mathbf{H}^{\mathrm{I}}\mathbf{u}^{\mathrm{I}}. \tag{3.10}$$

The perfect bonding between the prism and inhomogeneity is assumed, i.e., the conditions of continuity of displacements, and equilibrium of tractions are satisfied:

$$\mathbf{u}^{\mathrm{PI}} = \mathbf{u}^{\mathrm{I}}, \quad \mathbf{t}^{\mathrm{PI}} = -\mathbf{t}^{\mathrm{I}}. \tag{3.11}$$

Inserting (3.10) and (3.11) into (3.8) leads to:

$$\begin{bmatrix} \mathbf{L}_{11}^{\mathrm{P}} & \mathbf{L}_{12}^{\mathrm{P}} + \mathbf{R}_{12}^{\mathrm{P}}(\mathbf{G}^{\mathrm{I}})^{-1}\mathbf{H}^{\mathrm{I}} \\ \mathbf{L}_{21}^{\mathrm{P}} & \mathbf{L}_{22}^{\mathrm{P}} + \mathbf{R}_{22}^{\mathrm{P}}(\mathbf{G}^{\mathrm{I}})^{-1}\mathbf{H}^{\mathrm{I}} \end{bmatrix} \begin{Bmatrix} \mathbf{t}^{\mathrm{P}} \\ \mathbf{u}^{\mathrm{I}} \end{Bmatrix} = \begin{bmatrix} \mathbf{R}_{11}^{\mathrm{P}} \\ \mathbf{R}_{21}^{\mathrm{P}} \end{bmatrix} \left\{ \mathbf{u}^{\mathrm{P}} \right\}. \tag{3.12}$$

The final equation involve unknown tractions on the external boundary of the prism $\mathbf{t}_{\mathrm{P}}$ and displacements on the interface $\mathbf{u}_{\mathrm{I}}$. Tractions on the interface can be recovered (if necessary) in the postprocessing stage by using Eq. (3.10).

3.3. The fast multipole boundary element method

Matrices in the system of equations (3.5) are dense and nonsymmetric, and affect the efficiency of the method for large structures. The complexity of the conventional BEM is at least $O(N^2)$, where N denotes the number of degrees of freedom of the structure. Efficient versions of the BEM are available including the fast multipole BEM (FMBEM). The method is known to reduce the complexity to $O(N)$ or $O(N \log N)$ [35, 36].

The FMBEM algorithm uses a hierarchical grouping of boundary elements and collocation points and efficiently distributes integrals (potentials) over the groups. The grouping process is represented by a tree structure with the root at a level that corresponds to the whole domain. Far-field potentials are approximated by multipole expansions that involve solid harmonic functions [36]. Near-field potentials that correspond to the influence of closely located groups are calculated directly as in the conventional BEM. Thus, the matrix system of equations takes the form:

$$[\mathbf{L}^{\mathrm{near}}]\{\mathbf{y}\} + \{\mathbf{L}\mathbf{y}\}^{\mathrm{far}} = [\mathbf{R}^{\mathrm{near}}]\{\mathbf{z}\} + \{\mathbf{R}\mathbf{z}\}^{\mathrm{far}}, \tag{3.13}$$

in which $[\,\cdot\,]^{\mathrm{near}}$ matrices include the near-field integrals and $\{\,\cdot\,\}^{\mathrm{far}}$ vectors include far-field potentials that are calculated by using expansions and translations. For the single-inhomogeneity problem, the system of equations (3.12) is transformed to the form similar to (3.13), with potentials split up into near- and far-type terms. The system of equation is solved iteratively. A single iteration is composed of the following steps:

- Direct computation of the near-field potentials.
- Computation of multipole moments for the smallest groups.
- *Multipole-to-multipole* translations during the upward pass.
- *Multipole-to-local* translations.
- *Local-to-local* translations during the downward pass.
- Computation of the far-field potentials by the local series.

For the inhomogeneity-problem, Eq. (3.12) is transformed into the form similar to (3.13) and solved iteratively. More details on the present FMBEM and its applications in micromechanics can be found in [25, 37].

4. Numerical examples

4.1. Composites with spherical particles

Consider a composite material with a matrix made of epoxy reinforced with randomly distributed silica spherical particles. Elastic properties of the matrix are: Young's modulus $E_0 = 3.16$ GPa and Poisson's ratio $\nu_0 = 0.25$. Corresponding properties of particles are: $E_1 = 73.1$ GPa and $\nu_1 = 0.18$. The same material was analyzed in [7]. To give an example of an application of the mean-field/FMBEM approach, a single-inhomogeneity FMBEM model was developed. To properly approximate an infinite body, the particle volume was set to not exceed 0.001 of the volume of the homogeneous cubic prism [14]. 16×16 mesh of 8-node quadratic elements was applied for the discretization of a single wall of the prism, and 96 elements for the spherical particle (Figs. 3a and 3b). In the whole model, the number of elements and nodes was equal to 1 632 and 4 900, respectively. For the M-T/FMBEM scheme (2.6), 6 tests were performed according to boundary conditions (2.8). The strain concentration tensor was calculated numerically as the surface integral (2.10) over the particle boundary. For the interpolative scheme D-I/FMBEM (2.16), additional 6 tests were performed for the structure with permuted elastic properties of the matrix and particle.

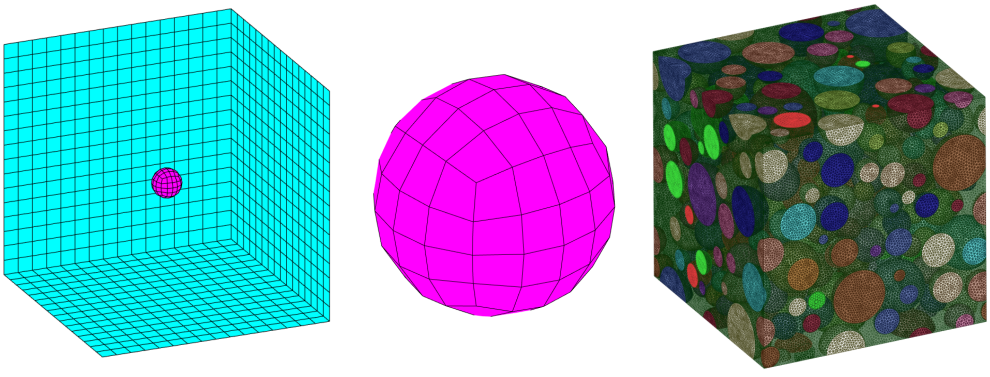

(a) (b) (c)

FIG. 3. Discretized models of the composite: a) interior of the BEM single-inhomogeneity model, b) boundary element mesh of the particle (mid-side nodes are skipped in the visualization), c) RVE/FEM model, $c_1 = 0.45$.

Computations were performed on a desktop PC equipped with the AMD Ryzen 5 2600 Six-Core 3.40 GHz CPU and 24 GB of RAM. The simulations utilized 4 parallel threads. The computation time for the dilute strain concentration tensor was approximately 3 minutes. It is important to note that the number of tests can be reduced due to the particle's symmetry. However, the general

procedure for arbitrary shapes requires 6 tests, and this research focused on validating the developed method. Overall, the preprocessing stage of the single inhomogeneity model and the computations were robust.

The reference numerical model for the composite was the representative volume element (RVE, [9]) generated and analysed by the Ansys/Material Designer software. RVEs with volume fraction of particles $c_1 \in \{0.05, 0.1, 0.15, 0.2, 0.25, 0.3, 0.35, 0.389, 0.45\}$ (for $c_1 = 0.389$, the numerical values of the elastic properties calculated are given in [7] and are used for the comparison). The number of particles ranges from 16 (for $c_1 = 0.05$) to 569 ($c_1 = 0.45$). Homogenization tests with periodic boundary conditions were performed. 10-node tetrahedral elements with quadratic shape functions were applied to the discretization. The finite element mesh was generated with default software settings. The software adjusts the mesh density to the particle size and distance between constituent boundaries and edges and assures that the mesh is periodic. The number of elements in the discretized models ranged from 163 355 to 3 426 853, and nodes from 231 192 to 4 686 512. A typical FEM/RVE model is shown in Fig. 3c. The total number of FEM simulations was 54, with the number of degrees of freedom in the discretized BVP problem $N \sim [10^5, 10^7]$. The FEM computations were parallelized to 4 threads, similar to the FMBEM. The computation time for a single RVE (6 homogenization tests) depends on c_1, and ranged from 4 to 94 minutes. The total FEM computation time was about 3 hours and 20 minutes and was substantially longer than 3 minutes for M-T/FMEBM and 6 minutes for D-I/FMBEM. Note that the reported time does not include the preprocessing stage (generating geometry and meshing) which is usually considered significant in the FEM modelling. For example, the meshing time for the RVE with $c_1 = 0.45$ was about 5 minutes. The process of saving the amount of data on disk is also relatively time-consuming.

The FEM software gives the output in the form of engineering constants (three Young's moduli, three shear moduli and three Poisson's ratios) or elements of the macro stiffness matrix. To eliminate the possible small yet present effect of the anisotropy of the modelled structures, mean values of corresponding moduli, which should be equal for isotropy, are presented here. Comparison of the computed normalized effective Young and shear moduli is shown in Figs. 4 and 5, respectively. The results are compared with the analytical models: Mori–Tanaka ('M-T/analytical') and self-consistent method in two versions. These versions assume Voigt (upper bound) or Reuss (lower bound) assumptions for the comparison medium and provide simple formulas for the approximated bounds (abbreviated to 'AB') for overall constants [38]. We refer to these methods as 'AB-Up/analytical' and 'AB-Low/analytical', respectively. The present mean-field/numerical approaches are referred to as:

- M-T/FMBEM – the Mori–Tanaka assumption for the original problem (2.6) with numerically computed strain concentration tensor,
- D-I/FMBEM – the numerical strain concentration tensor replaced with the interpolation (2.16) involving both original and the inverse Mori–Tanaka problem.

The M-T/FMBEM approach agrees very well with the M-T/analytical results for both moduli (Figs. 4 and 5). The results for $c_1 = 0.45$ agree within

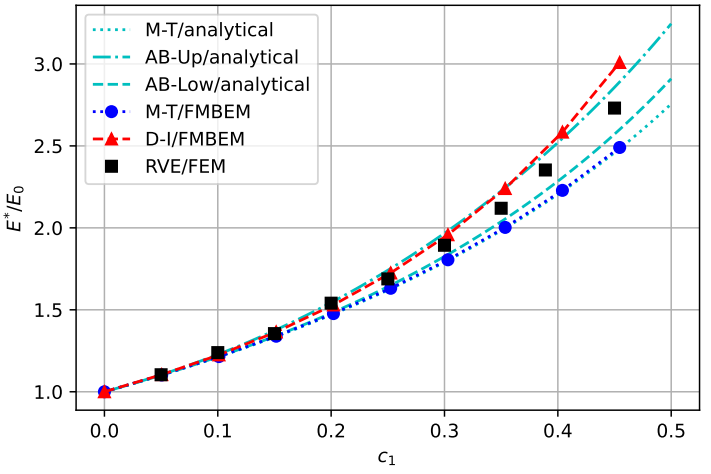

FIG. 4. Normalized effective Young's modulus of the spherical-particle reinforced composites.

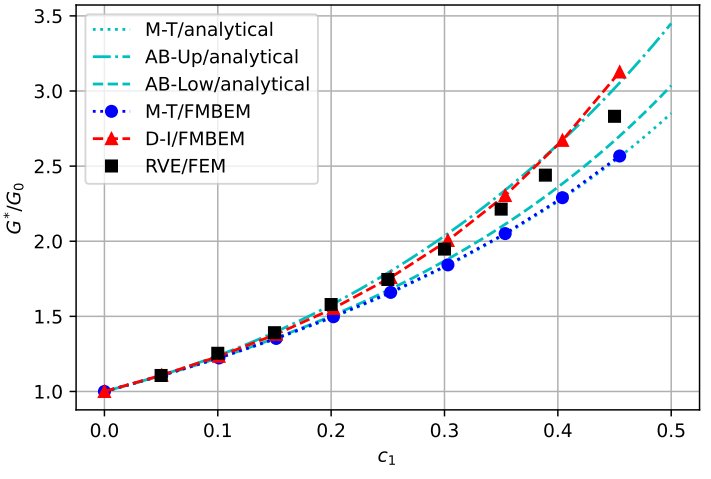

FIG. 5. Normalized effective shear modulus vs. volume fraction of particles of the spherical-particle reinforced composites.

the tolerance of 1%. Evidently, the strain concentration tensor is calculated with high accuracy. As expected, the M-T models underestimate the results in comparison to the RVE/FEM approach. The D-I/FMBEM is very close to the AB-Up/analytical result. Thus, the present mean-field/FMBEM approaches give expected results with minimal computational effort. For $c_1 = 0.389$, the numerical values are compared to the results from [7] in Table 1. In the paper, the original notion 'M-T' stands for the analytical Mori–Tanaka method and 'D-I' for the analytical double-inclusion interpolative scheme (2.16). For the M-T and D-I schemes, the relative difference for both moduli is less than 0.25%. In the FMBEM analysis, the amount of the discretized model data to be prepared and processed is much less than for the FEM, as the number of degrees of freedom is only $N \sim 10^4$ (against $N \sim [10^5, 10^7]$ for RVE/FEM) for the present example. The FEM always requires the discretization of the whole domain (Figs. 1b and 3a), which makes the method more demanding from the user point of view. Furthermore, the BEM offers easier preparation and possible manipulation with the model as the boundaries of the prism and inhomogeneity are meshed independently. The computation time for mean-field/FMBEM was substantially shorter compared to the FEM (3 or 6 minutes for M-T/FMBEM and D-I/FMBEM, versus over 3 hours for RVE/FEM).

TABLE 1. Effective elastic moduli of the epoxy/silica composite for $c_1 = 0.389$.

Modulus	M-T [7]	D-I [7]	RVE/FEM	M-T/FMBEM	D-I/FMBEM
E^* [GPa]	6.8194	7.7979	7.4357	6.8102	7.8180
G^* [GPa]	2.5875	2.9828	2.8556	2.5924	2.9890

4.2. Composites with randomly distributed and oriented cubic particles

A composite made of an aluminum alloy matrix and cubic silicon carbide particles was analyzed. For such a problem, one cannot apply analytical methods as they usually assume ellipsoidal shape of inclusions (inhomogeneities). Particles of the same size were randomly distributed. The elastic constants for the matrix are: $E_0 = 70$ GPa, $\nu_0 = 0.30$, and particles $E_1 = 415$ GPa, $\nu_1 = 0.16$. The corresponding FMBEM single-inhomogeneity model contained single cubic particle embedded in the cubic prism. The volume of the particle was the fraction 0.001 of the volume of the homogeneous prism. The boundary element mesh for a single wall of the prism contained 16×16 elements, and of the particle 4×4 elements. The boundary element mesh was composed of 1 632 elements and 4 900 nodes. The interior of the discretized model is shown in Fig. 6b, and magnified particle in Fig. 6b.

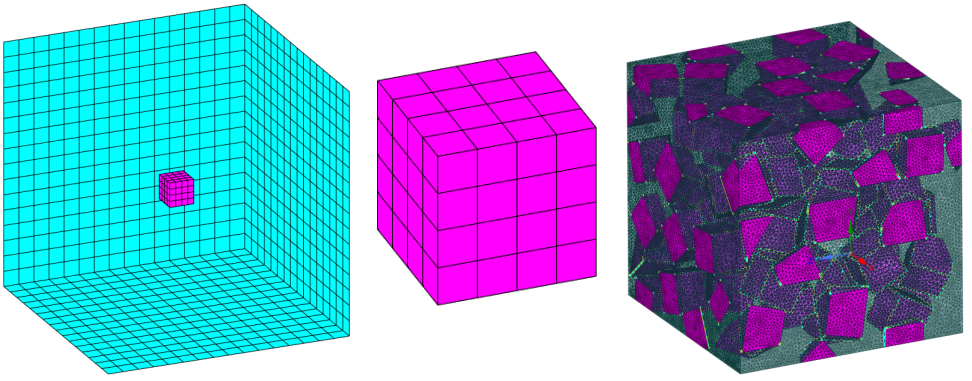

(a) (b) (c)

FIG. 6. Discretized models of the composite: a) interior of the BEM single-inhomogeneity model, b) boundary element mesh of the particle, c) the RVE/FEM model, $c_1 = 0.25$.

Both schemes were considered, i.e., the Mori–Tanaka scheme (6 tests for the direct problem) and the interpolative scheme that involves the additional Mori–Tanaka problem (additional 6 tests). For the calculation of the final effective elastic properties of the isotropic medium, averaging over orientations (2.14), (2.15) was performed. The same composite material was considered in [14] and analyzed by the hybrid Mori–Tanaka/FEM approach. The strain concentration tensor was calculated numerically by a model similar to Fig. 1b. Following the cited paper, we give the strain concentration tensor in the matrix notation. The FEM result of [14] is:

$$\mathbf{B}^{\mathrm{FEM}} = \begin{bmatrix} 0.34391 & 0.03273 & 0.03273 & 0 & 0 & 0 \\ 0.03273 & 0.34391 & 0.03273 & 0 & 0 & 0 \\ 0.03273 & 0.03273 & 0.34391 & 0 & 0 & 0 \\ 0 & 0 & 0 & 0.28037 & 0 & 0 \\ 0 & 0 & 0 & 0 & 0.28037 & 0 \\ 0 & 0 & 0 & 0 & 0 & 0.28037 \end{bmatrix}, \tag{4.1}$$

and the present FMBEM result:

$$\mathbf{B}^{\mathrm{FMBEM}} = \begin{bmatrix} 0.34540 & 0.03210 & 0.03210 & 0 & 0 & 0 \\ 0.03210 & 0.34540 & 0.03210 & 0 & 0 & 0 \\ 0.03210 & 0.03210 & 0.34540 & 0 & 0 & 0 \\ 0 & 0 & 0 & 0.28137 & 0 & 0 \\ 0 & 0 & 0 & 0 & 0.28137 & 0 \\ 0 & 0 & 0 & 0 & 0 & 0.28137 \end{bmatrix}. \tag{4.2}$$

The FMBEM strain concentration matrix agrees with the FEM as the maximum relative difference between the corresponding nonzero off-diagonal elements

of the matrix is less than 2%, and for diagonal elements less than 1%. However, the FEM requires discretization of the entire domain, and a reasonable transition between coarse mesh on the external boundary and fine mesh for the particle is required. On the contrary, the boundary element meshes of the corresponding boundaries for the present FMBEM model are independent of each other and easy to generate.

Reference models for the effective elastic moduli were RVEs generated in DIGIMAT software, which allows the user to model composites reinforced with any shape of particles defined by a separate CAD file. The volume fraction of the particles $c_1 \in \{0.05, 0.1, 0.15, 0.2, 0.25\}$. Number of particles ranged from 64 to 103. The models were discretized by 10-node tetrahedral finite elements with quadratic shape functions. The number of elements in models ranged from 1 112 144 to 1 997 470, and nodes from 1 529 075 to 2 749 291. The discretized model of the RVE with the highest c_1 is shown in Fig. 6c. For homogenization, six tests with periodic boundary conditions were applied. Thus, 30 boundary value problems with significant size $N \sim 10^6$, were solved. With the same computer setup as in the previous example and Ansys Material Designer applied to the analysis, the computation time for a single RVE (6 tests) ranged from 15 to 44 minutes. The total computation time of all RVEs was 147 minutes (almost 2.5 hours). As a result, the effective bulk (K^*) and shear (G^*) moduli of the homogenized material were calculated. The comparison of the results, normalized with corresponding moduli of the matrix material (K_0, G_0), is shown in Table 2, and Figs. 7 and 8.

TABLE 2. Efective elastic moduli of the composite with randomly oriented cubic particles.

c_1	RVE/FEM		M-T/FMBEM		D-I/FMBEM	
	K^*/K_0	G^*/G_0	K^*/K_0	G^*/G_0	K^*/K_0	G^*/G_0
0.05	1.05261	1.08379	1.05249	1.08604	1.05297	1.08707
0.10	1.10488	1.17879	1.10828	1.17861	1.11033	1.18306
0.15	1.16516	1.27542	1.16768	1.27847	1.17260	1.28931
0.20	1.23252	1.40272	1.23105	1.38654	1.24033	1.40734
0.25	1.30740	1.52779	1.29882	1.50385	1.31413	1.53889

For the effective moduli, both M-T/FMBEM and D-I/FMBEM results are close to the reference RVE/FEM, and the three-point approximation (TPA/analytical) with the assumption of stiff hexahedral particles in a deformable matrix [39, 40]. The difference between the present two mean-field approaches increases with the volume fraction c_1 to reach the relative difference in bulk modulus of 1.2%, and in shear modulus 2.3%, for $c_1 = 0.25$ (Table 2).

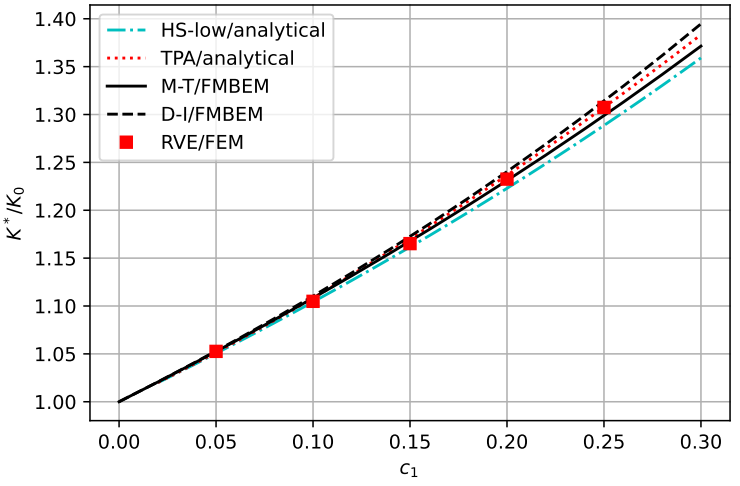

FIG. 7. Normalized effective bulk modulus of composites with randomly oriented cubic particles.

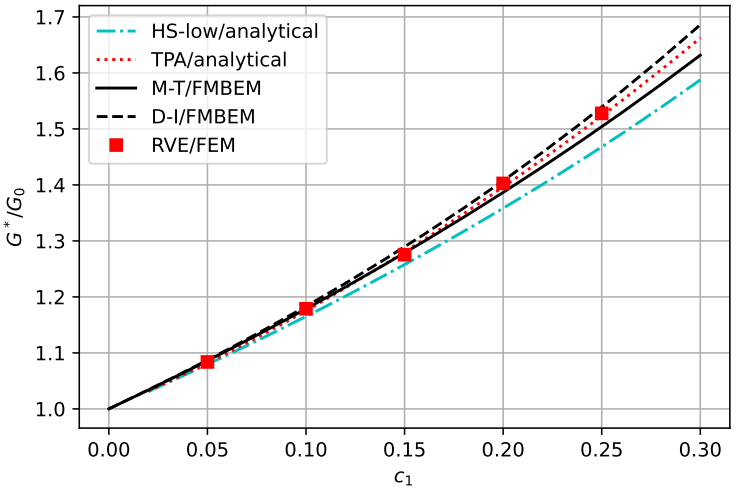

FIG. 8. Normalized effective shear modulus of composites with randomly oriented cubic particles.

All results are above (or close to, for small c_1) Hashin–Shtrikman lower bounds (HS/analytical) reported in [40]. Note that the FEM results may be affected by the number of particles in the RVE and FEM errors (geometry approximation, discretization, solution of the system of equations and others). Nevertheless, the FEM convergence study is difficult to perform due to relatively large models and the requirement of mesh periodicity.

Both mean-field/FMBEM approaches properly predict the trends of increasing effective elastic constants (Figs. 7 and 8) while offering minimized computational effort. Again, 12 discretized BVP problems with $N \sim 10^4$ were solved for two mean-field series of the results for the whole considered range of the volume fraction of the particles. The time of the computations of a single dilute strain concentration tensor was approximately 3 minutes. Accordingly, the D-I/FMBEM time was about 6 minutes. It is substantially less compared to over two hours as reported for the FEM/RVE.

4.3. Hybrid materials with auxetic aligned cubic subregions

We consider the design of a hybrid material composed of two phases. Young's moduli of both phases are equal: $E_0 = E_1 = 1$. Poisson's ratio: $\nu_0 = 0.45$ and $\nu_1 \in \langle -0.9; -0.1 \rangle$ with the step of 0.1. Thus, the phase '1' is auxetic. The auxetic subregions are aligned, randomly distributed cubes. Although the hybrid is not a inventional composite material, the model for composites may be applied here to estimate the effective elastic properties of such a structure. Due to the presence of the auxetic component, the overall structure behaves in a nonconventional manner, i.e., it has a local maximum of the effective Young's modulus expressed as a function of the volume fraction c_1 [27, 28].

For the geometry of the single-inhomogeneity problem solved by the FMBEM, exactly the same discretized model as in the previous example was applied (Fig. 6). Again, the boundary element mesh was composed of 1 632 elements and 4 900 nodes. Preliminary results showed that the M-T/FMBEM scheme improperly predicts the maximum of the Young modulus (see Appendix for the results). Therefore, the D-I/FMBEM scheme was applied for each value of ν_1, i.e., two strain concentration tensors were calculated for each case (18 in total; 108 FMBEM simulations). The time of calculation of the single tensor was about 3 minutes. The total time of D-I/FMBEM calculations was about one hour.

For the validation of the results, FEM/RVE models were generated based on the idea proposed in [27]. Each RVE was a cube composed of aligned smaller cubes with properties randomly chosen to refer to phase '0' or '1'. The RVE contained 5×5×5 such smaller cubes. The small cube was discretized by 6×6×6 20-node hexahedral elements. The mesh density was determined on the basis of the study reported in [27]. The model had 27 000 elements and 116 281 nodes. A typical RVE is shown in Fig. 9. Ten random RVEs were generated for each value of $c_1 \in \langle 0.1; 0.9 \rangle$ with a step 0.1, and additionally for $c_1 = 0.95$. Periodic boundary conditions with six standard homogenization tests were applied. Thus, a total of 900 RVEs were analyzed (which involved 5 400 FEM simulations). Models were generated, solved and postprocessed using Python scripts and the PyAnsys/PyMAPDL package. FEM computations were parallelized

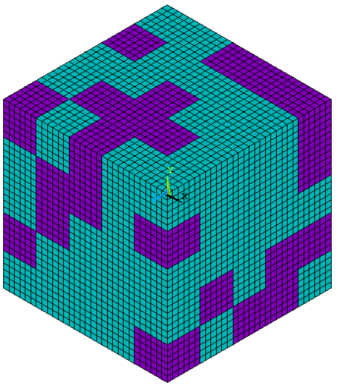

FIG. 9. Typical RVE/FEM model of the hybrid material.

into 6 threads. In this case, the overall time of 6 homogenization tests of a single RVE was recorded, including the whole process. The time was approximately 42 minutes and is relatively long due to the PyMAPDL preparation of the models for the RVE analysis with periodic boundary conditions. Still, multiple parameterized FEM analyses require preparation and processing of the amount of data, and Python scripting helps easy automation of this task.

By utilizing the FEM models, the effective Young modulus and shear modulus were derived from the effective compliance, which represents the inverse of the material's stiffness. The results showed that the structures are isotropic. This is caused by the fact that the elastic contrast between phases is close to unity. The normalized results for these moduli are presented in Figs. 10 and 11, respectively. According to both RVE/FEM and D-I/FMBEM models, the effective Young modulus of the hybrid reaches its local maximum $\hat{E}^*$ in the approximate range of $c_1 \in \langle 0.6, 0.7 \rangle$ (Fig. 10). The maximum increases with the decrease of ν_1 to reach the normalized value $\hat{E}^*/E_0 \approx 3$ when the auxetic material is close to the thermodynamic limit, i.e., $\nu_1 = -0.9$. This result agrees with [27]. However, here, more values of ν_1 are investigated. In the case of RVE/FEM, the spread of the results of 10 random RVEs gets wider for lower ν_1. The spread is more visible near the Young's modulus optimum. On the other hand, for ν_1 closer to 0, the spread caused by the random geometry of the RVEs is negligible. Lower differences between the RVE/FEM and D-I/FMBEM results are observed as well. For the shear modulus, the spread of results caused by the random geometry of the RVE is also wider near the optimum of the effective Young modulus (Fig. 11), i.e., for c_1 close to 0.6 or 0.7. Again, the width of the ranges decreases with increasing ν_1.

To give more details on the numerical results, the computed values of maximum Young's modulus are gathered in Table 3. For the RVE/FEM, ranges and mean values are given. The results confirm the observed dependence of the spread

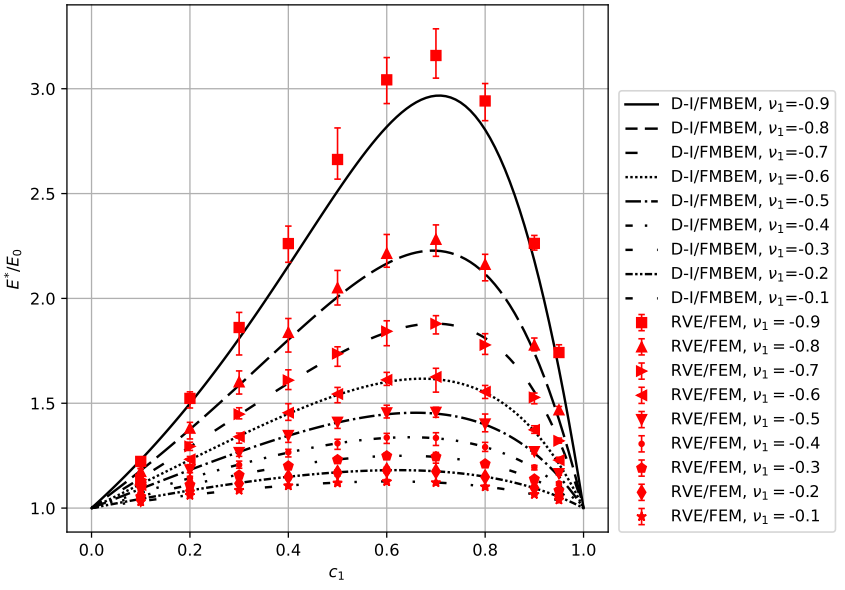

FIG. 10. Normalized effective Young's modulus of the hybrid material.

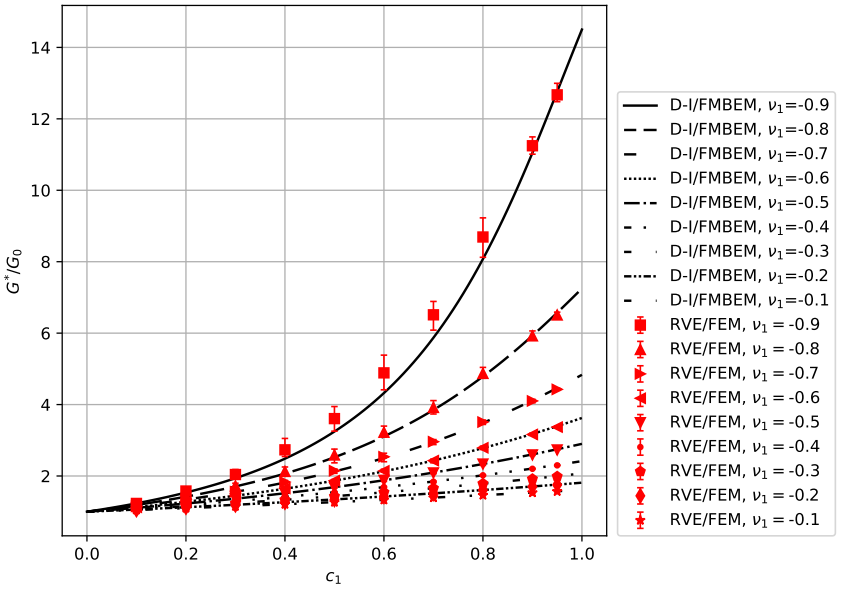

FIG. 11. Normalized effective shear modulus of the hybrid material.

of the effective moduli calculated by RVE/FEM. The width of the interval related to the mean value is: 7.2% for $c_1 = -0.9$ and 2% for $c_1 = -0.1$. In addition to the numerical values of the moduli, Table 3 shows the actual value of the position

of its maximum calculated by RVE/FMBEM: $\hat{c}_1 \in \{0.6; 0.7\}$, and D-I/FMBEM: $\hat{c}_1 \in \langle 0.61; 0.71 \rangle$. The maximum relative difference in Young's modulus between the mean RVE/FEM and D-I/FMBEM results is observed for $\nu_1 = -0.9$ and is about 6%. The respective difference for $\nu_1 = -0.1$ is less than 0.01%.

This example shows that the proposed mean-field/FMBEM approach can be efficiently applied to design new hybrid materials. A total of 108 D-I/FMBEM simulations with lower number degrees of freedom ($N \sim 10^4$) against 5 400 RVE/FEM simulations ($N \sim 10^5$) were run to obtain comparable results capturing the maximum of the hybrid material. The D-I/FMBEM overall time, i.e., for all material constant combinations, was comparable to the analysis of just a single RVE modelled by the FEM and pre- and postprocessed by using PyMAPDL (one hour versus about 42 minutes). Analyses of many RVE/FEM models require much more effort than the mean-field/FMBEM approach. Thus, the proposed approach can be applied to efficiently explore the space of properties of new materials, including hybrids with auxetic phases, although the modelling has to be performed carefully due to possible inaccuracy of Mori–Tanaka predictions.

TABLE 3. Optimized effective Young's modulus of the hybrid material.

ν_1	RVE/FEM				D-I/FMBEM	
	$\min(\hat{E}^*/E_0)$	$\max(\hat{E}^*/E_0)$	$\text{mean}(\hat{E}^*/E_0)$	$\hat{c}_1$	$\hat{E}^*/E_0$	$\hat{c}_1$
−0.1	1.11641	1.13854	1.12621	0.6	1.12707	0.61
−0.2	1.16605	1.19367	1.18028	0.6	1.18090	0.62
−0.3	1.23412	1.26388	1.24893	0.6	1.24944	0.63
−0.4	1.31628	1.36421	1.33630	0.6	1.33785	0.65
−0.5	1.43262	1.48009	1.45661	0.7	1.45466	0.66
−0.6	1.58419	1.69782	1.62543	0.7	1.61707	0.67
−0.7	1.84081	1.92799	1.87927	0.7	1.87992	0.70
−0.8	2.21331	2.36322	2.28196	0.7	2.22785	0.69
−0.9	3.03128	3.26649	3.15850	0.7	2.96723	0.71

4.4. Comparison of averaged strains computed by different approaches

A comparison of averaged strains over phases computed by different approaches was performed. For the FEM, strains in the centroid of finite elements $\check{\varepsilon}^e_{ij}$ were extracted and applied to the averaging over phases similar to [10]:

$$\langle \varepsilon_{ij} \rangle_{\Omega_{0,1}} \approx \frac{\sum_{e=1}^{Q} \check{\varepsilon}^e_{ij} \check{V}^e}{\sum_{e=1}^{Q} \check{V}^e}, \tag{4.3}$$

where Q is the number of finite elements used to discretize corresponding phase: Ω_0 (matrix) or Ω_1 (particles). $\check{V}^e$ is the volume of the eth element in

the phase. In the M-T/FMBEM and D-I/FMBEM calculations, corresponding dilute concentration tensor $\boldsymbol{B}$ (2.11) or (2.16), and Eqs. (2.3) and (2.5) were applied. A comparison of averaged strains over composite phase computed by RVE/FEM, M-T/FMBEM and D-I/FMBEM for structures from the previous sections with the highest differences between effective moduli predictions is presented in Tables 4, 5 and 6 and Figs. 12, 13 and 14. In the case of RVE/FEM, probability density histograms are also presented. Table 7 contains a comparison of the standard deviation of the strains computed by RVE/FEM in the phases of the materials.

TABLE 4. Average strains in the composite with spherical particles for $c_1 = 0.45$ and $\bar{\varepsilon}_{11,23} = 10^{-3}$.

Phase	$\langle \varepsilon_{11} \rangle$			$\langle \varepsilon_{23} \rangle$		
	RVE/FEM	M-T/FMBEM	D-I/FMBEM	RVE/FEM	M-T/FMBEM	D-I/FMBEM
Ω_1	1.81631e-4	1.60143e-4	2.28406e-4	1.60245e-4	1.34431e-4	1.93583e-4
Ω_0	1.66986e-3	1.68716e-3	1.63130e-3	1.68737e-3	1.70819e-3	1.65980e-3

TABLE 5. Average strains in the composite with randomly oriented cubic particles for $c_1 = 0.25$ and $\bar{\varepsilon}_{11,23} = 10^{-3}$.

Phase	$\langle \varepsilon_{11} \rangle$			$\langle \varepsilon_{23} \rangle$		
	RVE/FEM	M-T/FMBEM	D-I/FMBEM	RVE/FEM	M-T/FMBEM	D-I/FMBEM
Ω_1	4.25810e-4	4.12330e-4	4.70315e-4	3.70921e-4	3.42990e-4	3.97530e-4
Ω_0	1.19140e-3	1.19589e-3	1.17656e-3	1.20969e-3	1.21900e-3	1.20082e-3

TABLE 6. Average strains in phases of the hybrid material for $c_1 = 0.7$, $\nu_1 = -0.9$ and $\bar{\varepsilon}_{11,23} = 10^{-3}$.

Phase	$\langle \varepsilon_{11} \rangle$			$\langle \varepsilon_{23} \rangle$		
	RVE/FEM	M-T/FMBEM	D-I/FMBEM	RVE/FEM	M-T/FMBEM	D-I/FMBEM
Ω_1	8.00273e-4	7.18744e-4	8.97761e-4	5.83671e-4	3.76710e-4	6.64330e-4
Ω_0	1.45727e-3	1.65626e-3	1.23856e-3	1.95317e-3	2.45433e-3	1.78324e-3

One can assess the predicted mean strains over phases by comparing the difference between RVE/FEM and mean-field/FMBEM strain results normalized by $\bar{\varepsilon}_{11,23} = 0.001$. Accordingly, for the composite with spherical particles, the maximum normalized difference is observed between RVE/FEM and D-I/FMBEM and equals 4.68% (particles, normal-strain test) and 3.86% (matrix, normal strain test). The M-T/FMBEM approach gives slightly closer values to RVE/FEM average strains as the difference in all cases does not exceed 2.6%.

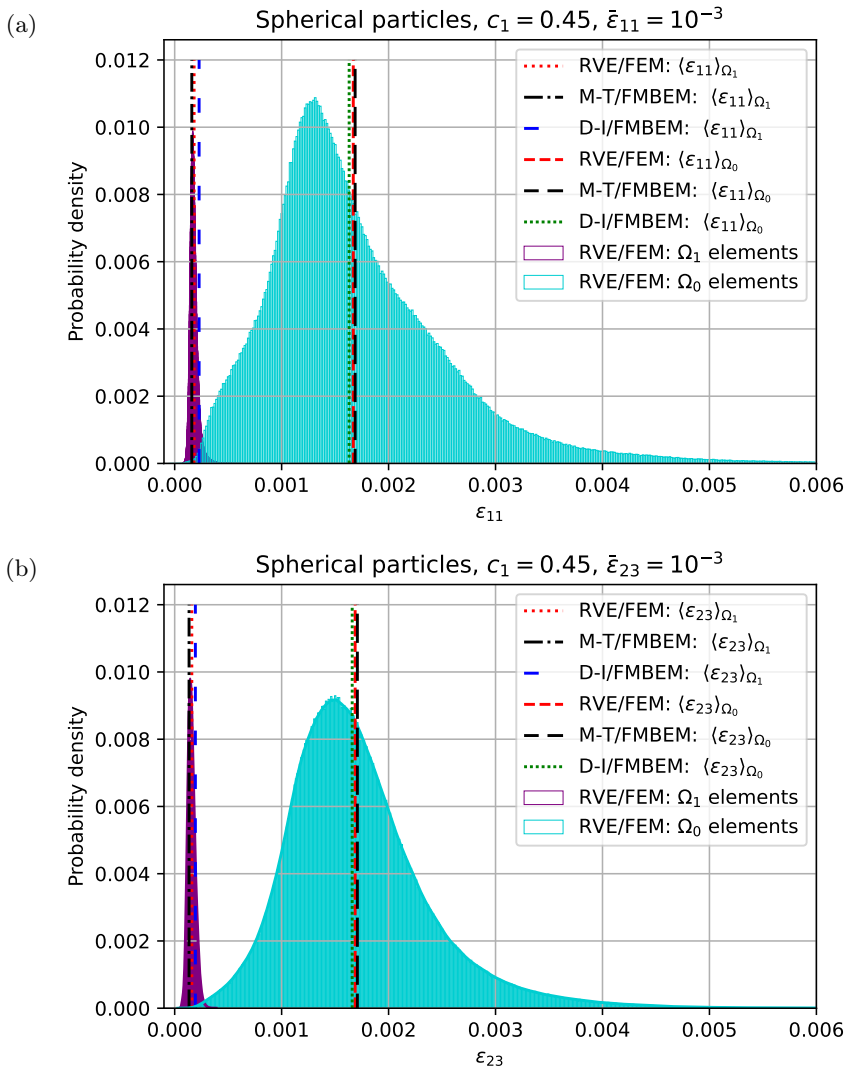

FIG. 12. Composite with spherical particles: probability densities of strains over particle and matrix finite elements in typical RVE model, and average strains in constituents computed by different approaches for $c_1 = 0.45$ and: a) $\bar{\varepsilon}_{11} = 10^{-3}$, b) $\bar{\varepsilon}_{23} = 10^{-3}$ (in each case remaining components of $\bar{\varepsilon}$ are equal to 0).

The differences between the normal-strain and shear-strain tests are comparable (Table 4, Fig. 12). For the composite with cubic particles, the maximum normalized difference is also observed between RVE/FEM and D-I/FMBEM and equals 4.45% (particles, normal-strain test) and 1.48% (matrix, normal-strain test). The corresponding maximum difference for M-T/FMBEM–RVE/FEM results does not exceed 2.8% (shear test, particles). Similarly to the composite with

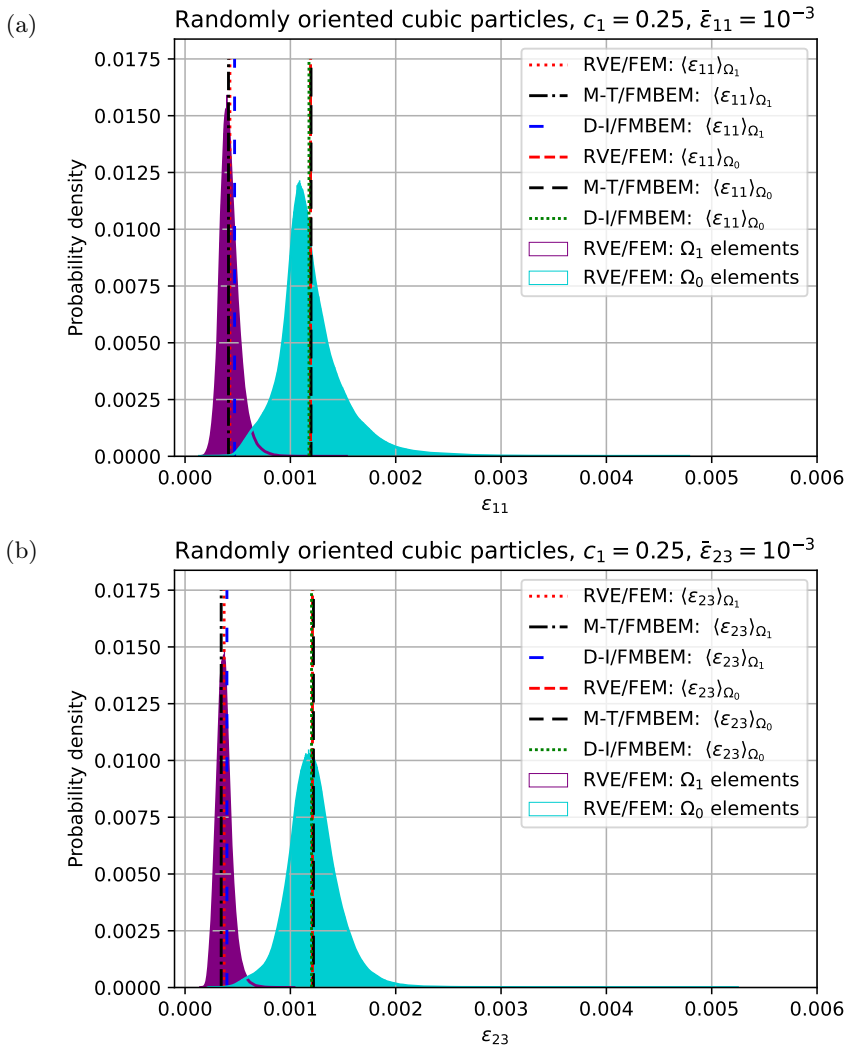

FIG. 13. Composite with randomly oriented cubic particles: probability densities of strains over particle and matrix finite elements in typical RVE model, and average strains in constituents computed by different approaches for $c_1 = 0.25$ and: a) $\bar{\varepsilon}_{11} = 10^{-3}$, b) $\bar{\varepsilon}_{23} = 10^{-3}$ (in each case remaining components of $\bar{\varepsilon}$ are equal to 0).

spherical particles, the differences in the normal-strain and shear-strain tests are comparable. The assumption of mean strains is acceptable for the conventional composites, reinforced with spherical and cubic particles within the considered range of volume fractions. The corresponding vertical lines in Figs. 12 and 13 almost overlap. However, the standard deviation for FEM/RVE averaged

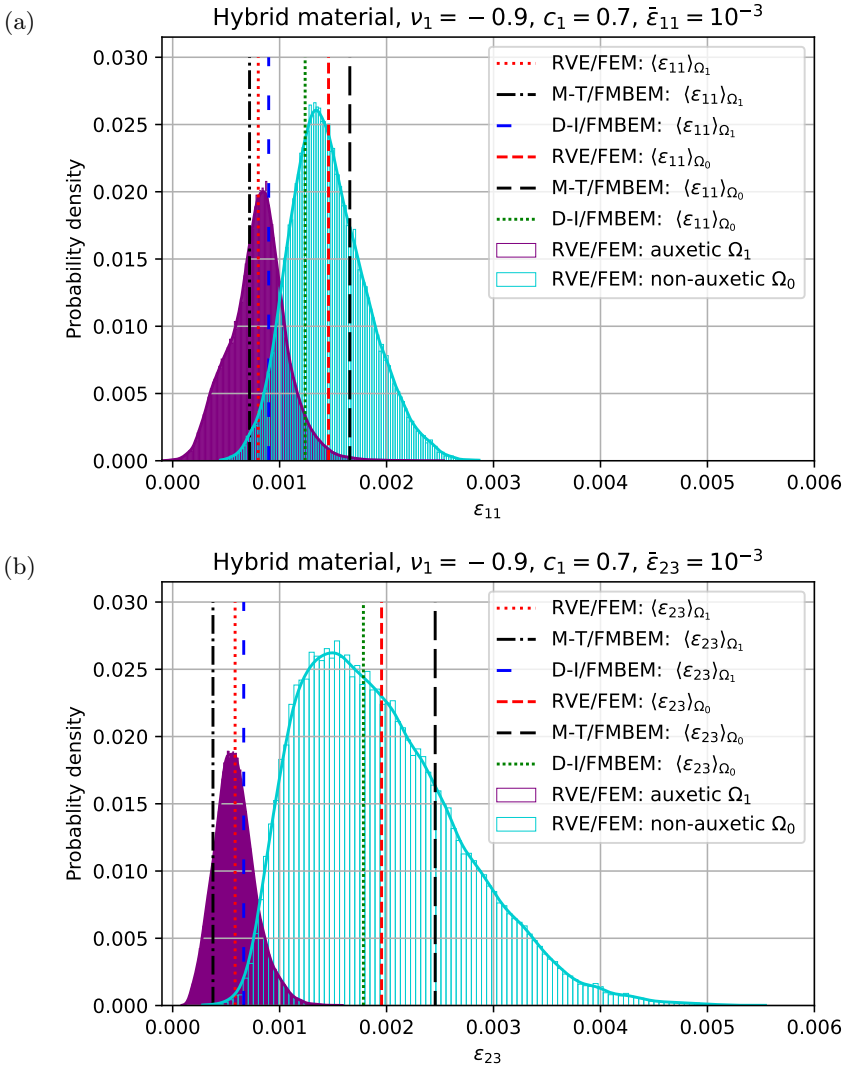

FIG. 14. Hybrid material: probability densities of strains over particle and matrix finite elements in typical RVE model, and average strains in constituents computed by different approaches for $c_1 = 0.7$, $\nu_1 = -0.9$ and: a) $\bar{\varepsilon}_{11} = 10^{-3}$, b) $\bar{\varepsilon}_{23} = 10^{-3}$ (in each case remaining components of $\bar{\varepsilon}$ are set to 0).

strains in cubic particles is higher than for spherical ones (Table 7). Thus, there is a wider spread of strains from the mean value in cubic particles than in spherical ones yet for lower volume fractions of the reinforcement (Figs. 12 and 13).

In the case of the hybrid material, the differences in mean strains are much higher. Accordingly, the normalized 'M-T/FMBEM–RVE/FEM' difference ranges from 20.7% (particles, shear-strain test) to even 50.12% (matrix, shear-

TABLE 7. Standard deviation of strains $\breve{\varepsilon}^{e}_{11,23}$ in the RVE/FEM models considered in this section (Figs. 12, 13 and 14).

Composite type	c_1	Strain test	Particles (Ω_1)	Matrix (Ω_0)
Spherical particles	0.45	$\bar{\varepsilon}_{11}$=1e-3	3.93674e-5	8.71087e-4
		$\bar{\varepsilon}_{23}$=1e-3	3.56887e-5	6.59923e-4
Randomly oriented cubic particles	0.25	$\bar{\varepsilon}_{11}$=1e-3	9.21305e-5	3.14276e-4
		$\bar{\varepsilon}_{23}$=1e-3	7.18191e-5	2.43658e-4
Hybrid material	0.7	$\bar{\varepsilon}_{11}$=1e-3	2.63011e-4	3.53882e-4
		$\bar{\varepsilon}_{23}$=1e-3	1.90400e-4	7.40015e-4

strain test), Table 6. The results correspond to inaccurate predictions of the maximum effective Young modulus presented in Appendix. In the case of D-I/FMBEM, the difference ranges from 8.07% (particles, shear-strain test) to 21.87% (matrix, normal-strain test). The lower differences in mean strains explain better accuracy of the D-I/FMBEM in predicting the effective moduli of the hybrid material compared to the M-T/FMBEM approach. The auxetic phase behaves similarly to reinforcement particles in conventional composites – they undergo lower strains than the non-auxetic (matrix) phase. The spread of strains from mean values in the particle (auxetic) phase is the widest from the compared cases (Fig. 14 and Table 7). Therefore, careful consideration is essential when modelling hybrid materials with auxetic phases using the mean-field approach, though such modelling can be feasible and efficient.

5. Conclusions

The fast multipole boundary element method (FMBEM) for 3-D elasticity was combined with the mean-field approach: Mori–Tanaka and the interpolative scheme [26], to efficiently homogenize particulate composites. The FMBEM was applied to solve the single-inhomogeneity problem to calculate the strain concentration tensor. As opposed to the widely applied finite element method (FEM), the FMBEM uses only the discretization of the boundary of the structure. Three examples were considered: composites with randomly distributed spherical particles, composites with randomly distributed and oriented cubic particles, and hybrid materials with aligned and randomly distributed cubic auxetic subregions. The models were validated by analytical methods, numerical results from the literature, and homogenization with the use of representative volume elements (RVEs) modeled by the FEM. The average strains predicted by the mean-field approaches were compared to RVE/FEM models. Corresponding averaged values coincide for the conventional composites reinforced with spherical and cubic particles, whereas careful consideration is crucial when modelling

hybrid materials with auxetic phases due to higher differences, especially for the M-T/FMBEM approach. The prediction can be enhanced using the inverse Mori–Tanaka method along with an interpolation of strain concentration tensors found in the literature.

The proposed mean-field/FMBEM approach offers a significant reduction of the modeling effort, compared with the FEM/RVE analysis, by the decrease in the number of boundary value problems to be solved, their size, computation time and the simplification of meshing. Although efficient, the proposed approach is limited to perfectly bonded, isotropic, and linear elastic constituents. On the other hand, an extension of the application range is possible by the application of existing BEM formulations for anisotropy, inelastic materials, contact, or coupling with the FEM. Efficient application of the FMBEM in the contribution tensor approach, which involves the solution of the single-inhomogeneity problem, is also possible.

Appendix. M-T/FMBEM predictions of elastic moduli for the hybrid material

The Appendix contains M-T/FMBEM and inverse Mori–Tanaka/FMBEM (I-M-T/FMBEM) results for the hybrid material analyzed in the last example (Section 4.3). For the comparison, only three values of ν_1 were selected: -0.1, -0.5 and -0.9, for clarity. Results for normalized Young's and shear moduli are presented in Figs. 15 and 16. The D-I/FMBEM models were validated by RVE/FEM analyses in Section 4.3. The M-T/FMBEM approach, does not predict the optimum value of Young's modulus correctly, for lower values of ν_1. However, it agrees with both RVE/FEM and D-I/FMBEM for $c_1 < 0.1$. On the other hand, the inverse I-M-T/FMBEM related to the dilute strain concentration $\boldsymbol{B}_u$ (see in Section 2 for its definition) agrees with the RVE/FEM predictions for $c_1 > 0.9$. According to the interpolative scheme (2.16) and (2.17), for small c_1 the M-T approach is dominant in the solution, and on the other hand for high c_1, the inverse Mori–Tanaka method dominates. The observed behaviour of the predictions can be explained by the fact that the Mori–Tanaka approach is well suited for composites with small volume fractions of inhomogeneities with matrix-inclusion topology. For volume fractions close to 50% the topology of composite materials changes to the interwoven type, which is not well described by the Mori–Tanaka approaches.

Both M-T and I-M-T predict different optimum for the effective Young modulus. Only the combination of these two methods by using the interpolation function gives results comparable to the RVE/FEM models. Clearly, the predictions of effective moduli for intermediate values of c_1 are influenced by the interpolation function. Note that the interpolation function (2.17) is an arbitrary choice.

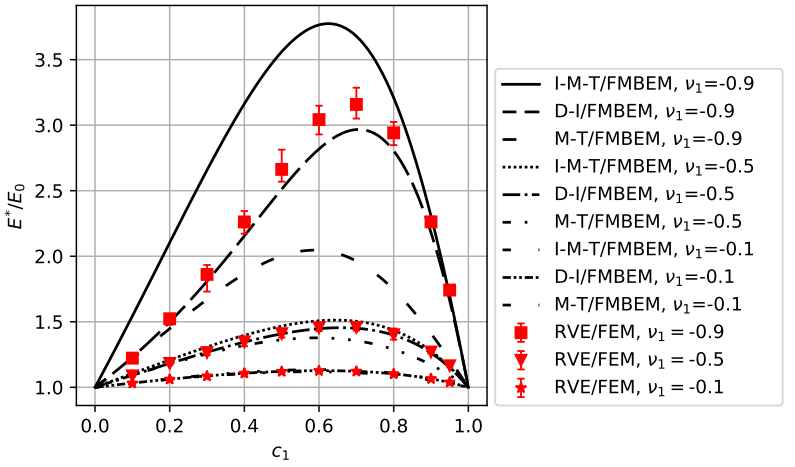

FIG. 15. Normalized effective Young's modulus of the hybrid material computed by different mean-field approaches.

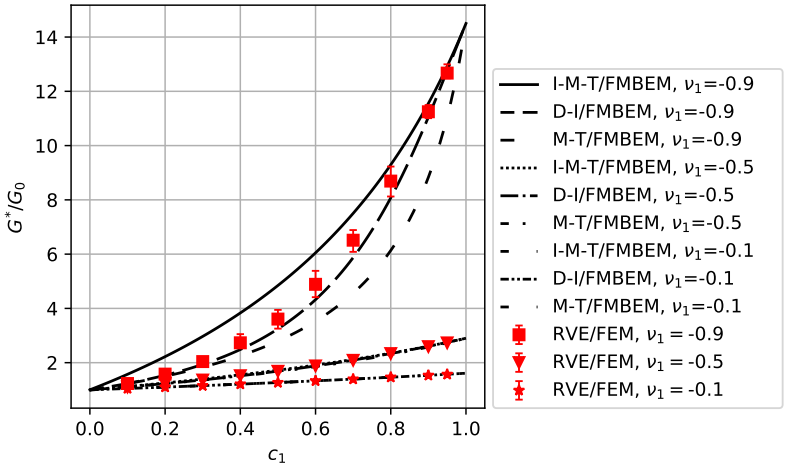

FIG. 16. Normalized effective shear modulus of the hybrid material computed by different mean-field approaches.

The effect of different optimal values predicted by various mean-field approaches decreases as the Poisson ratio ν_1 increases (the auxetic behavior of phase '1' gets weaker). For Poisson's ratio of -0.1, the three approaches yield nearly identical results. Similar trends can be observed regarding the shear modulus. The greatest discrepancy in the shear modulus results occurs at intermediate values of c_1. Additionally, a comparable phenomenon of expanding bounds with decreasing Poisson's ratio of the auxetic phase ν_1 was reported in [27].

Acknowledgements

The scientific research was funded from the statutory subsidy of the Faculty of Mechanical Engineering, Silesian University of Technology, Poland.

References

1. J.D. ESHELBY, *The determination of the elastic field of an ellipsoidal inclusion, and related problems*, Proceedings of the Royal Society A, **241**, 1226, 376–396, 1957, https://doi.org/10.1098/rspa.1957.0133.
2. T. MORI, K. TANAKA, *Average stress in matrix and average elastic energy of materials with misfitting inclusions*, Acta Metallurgica, **21**, 571–574, 1973, https://doi.org/10.1016/0001-6160(73)90064-3.
3. Y. BENVENISTE, *A new approach to the application of Mori–Tanaka's theory in composite materials*, Mechanics of Materials, **6**, 147–157, 1987, https://doi.org/10.1016/0167-6636(87)90005-6.
4. T. CHEN, G.J. DVORAK, Y. BENVENISTE, *Mori–Tanaka estimates of the elastic moduli of certain composite materials*, Journal of Applied Mechanics, **59**, 3, 539–546, 1992, https://doi.org/10.1115/1.2893757.
5. T. MURA, *Micromechanics of Defects in Solids*, Kluwer Academic Publishers, Dordrecht, 1987, https://doi.org/10.1007/978-94-009-3489-4.
6. S. NEMAT-NASSER, M. HORI, *Micromechanics: Overall Properties of Heterogeneous Materials*, Elsevier, Amsterdam, 1999.
7. O. PIERARD, C. FRIEBEL, I. DOGHRI, *Mean-field homogenization of multi-phase thermo-elastic composites: a general framework and its validation*, Composites Science and Technology, **64**, 10–11, 1587–1603, 2004, https://doi.org/10.1016/j.compscitech.2003.11.009.
8. J. QU, M. CHERKAOUI, *Fundamentals of Micromechanics of Solids*, John Wiley & Sons, New Jersey, 2006, https://doi.org/10.1002/9780470117835.
9. T.I. ZOHDI, P. WRIGGERS, *An Introduction to Computational Micromechanics*, Springer-Verlag, Berlin–Heidelberg, 2008, https://doi.org/10.1007/978-3-540-32360-0.
10. R.D. BRADSHAW, F.T. FISHER, L.C. BRINSON, *Fiber waviness in nanotube-reinforced polymer composites – II: modeling via numerical approximation of the dilute strain concentration tensor*, Composites Science and Technology, **63**, 11, 1705–1722, 2003, https://doi.org/10.1016/S0266-3538(03)00070-8.
11. L. BRASSART, I. DOGHRI, L. DELANNAY, *Homogenization of elasto-plastic composites coupled with a nonlinear finite element analysis of the equivalent inclusion problem*, International Journal of Solids and Structures, **47**, 5, 716–729, 2010, https://doi.org/10.1016/j.ijsolstr.2009.11.013.
12. G. SRINIVASULU, R. VELMURUGAN, S. JAYASANKAR, *A hybrid method for computing the effective properties of composites containing arbitrarily shaped inclusions*, Computers & Structures, **150**, 63–70, 2015, https://doi.org/10.1016/j.compstruc.2014.12.010.
13. P. SADOWSKI, K. KOWALCZYK-GAJEWSKA, S. STUPKIEWICZ, *Consistent treatment and automation of the incremental Mori–Tanaka scheme for elasto-plastic composites*, Computational Mechanics, **60**, 493–511, 2017, https://doi.org/10.1007/s00466-017-1418-z.

14. W. Ogierman, *Hybrid Mori–Tanaka/Finite Element Method in homogenization of composite materials with various reinforcement shape and orientation*, International Journal for Multiscale Computational Engineering, **17**, 3, 281–295, 2019, https://doi.org/10.1615/IntJMultCompEng.2019028827.

15. W. Ogierman, *A new model for time-efficient analysis of nonlinear composites with arbitrary orientation distribution of fibres*, Composite Structures, **273**, 114310, 2021, https://doi.org/10.1016/j.compstruct.2021.114310.

16. W. Ogierman, *A data-driven model based on the numerical solution of the equivalent inclusion problem for the analysis of nonlinear short-fibre composites*, Composites Science and Technology, **250**, 110516, 2024, https://doi.org/10.1016/j.compscitech.2024.110516.

17. O. Eroshkin, I. Tsukrov, *On micromechanical modeling of particulate composites with inclusions of various shapes*, International Journal of Solids and Structures, **42**, 2, 2005, https://doi.org/10.1016/j.ijsolstr.2004.06.045.

18. A. Trofimov, B. Drach, I. Sevostianov, *Effective elastic properties of composites with particles of polyhedral shapes*, International Journal of Solids and Structures, **120**, 157–170, 2017, https://doi.org/10.1016/j.ijsolstr.2017.04.037.

19. A. Markov, A. Trofimov, I. Sevostianov, *A unified methodology for calculation of compliance and stiffness contribution tensors of inhomogeneities of arbitrary 2D and 3D shapes embedded in isotropic matrix – open access software*, International Journal of Engineering Science, **157**, 103390, 2020, https://doi.org/10.1016/j.ijengsci.2020.103390.

20. Q.H. Qin, *Micromechanics–BE solution for properties of piezoelectric materials with defects*, Engineering Analysis with Boundary Elements, **28**, 7, 809–814, 2004, https://doi.org/10.1016/j.enganabound.2003.12.006.

21. Q.H. Qin, *Material properties of piezoelectric composites by BEM and homogenization method*, Composite Structures, **66**, 1–4, 295–299, 2004, https://doi.org/10.1016/j.compstruct.2004.04.051.

22. G. Dziatkiewicz, *Analysis of effective properties of piezocomposites by the subregion BEM–Mori–Tanaka approach*, Mechanics and Control, **30**, 4, 194–202, 2011.

23. P. Fedeliński, R. Górski, G. Dziatkiewicz, J. Ptaszny, *Computer modelling and analysis of effective properties of composites*, Computer Methods in Materials Science, **11**, 1, 3–8, 2011.

24. T. Czyż, G. Dziatkiewicz, P. Fedeliński [ed.], R. Górski, J. Ptaszny, *Advanced Computer Modelling in Micromechanics*, Silesian University of Technology Press, Gliwice, 2013.

25. J. Ptaszny, *A fast multipole BEM with higher-order elements for 3-D composite materials*, Computers & Mathematics with Applications, **82**, 148–160, 2021, https://doi.org/10.1016/j.camwa.2020.10.024.

26. G. Lielens, P. Pirotte, A. Couniot, F. Dupret, R. Keunings, *Prediction of thermo-mechanical properties for compression moulded composites*, Composites Part A: Applied Science and Manufacturing, **29**, 1–2, 63–70, 1998, https://doi.org/10.1016/S1359-835X(97)00039-0.

27. I. Shufrin, E. Pasternak, A.V. Dyskin, *Hybrid materials with negative Poisson's ratio inclusions*, International Journal of Engineering Science, **89**, 100–120, 2015, https://doi.org/10.1016/j.ijengsci.2014.12.006.

28. K. Long, X. Du, S. Xu, Y.M. Xie, *Maximizing the effective Young's modulus of a composite material by exploiting the Poisson effect*, Composite Structures, **153**, 593–600, 2016, https://doi.org/10.1016/j.compstruct.2016.06.061.

29. J. SCHJØDT-THOMSEN, R. PYRZ, *The Mori–Tanaka stiffness tensor: diagonal symmetry, complex fibre orientations and non-dilute volume fractions*, Mechanics of Materials, **33**, 10, 531–544, 2001, https://doi.org/10.1016/S0167-6636(01)00072-2.

30. C.A. BREBBIA, J. DOMINGUEZ, *Boundary Elements an Introductory Course*, McGraw-Hill, New York, 1992.

31. T. BURCZYŃSKI, *Boundary Element Method in Mechanics*, Scientific and Technical Publishing WNT, Warsaw, 1995 (in Polish).

32. X.W. GAO, G. DAVIES, *Boundary Element Programming in Mechanics*, Cambridge University Press, Cambridge, 2002.

33. G. BEER, I. SMITH, C. DUENSER, *The Boundary Element Method with Programming for Engineers and Scientists*, Springer–Verlag, Wien–New York, 2008, https://doi.org/10.1007/978-3-211-71576-5.

34. Z. YAO, F. KONG, X. ZHENG, *Simulation of 2D elastic bodies with randomly distributed circular inclusions using the BEM*, Electronic Journal of Boundary Elements, **1**, 2, 270–282, 2003, https://doi.org/10.14713/ejbe.v1i2.761.

35. L. GREENGARD, V. ROKHLIN, *A fast algorithm for particle simulations*, Journal of Computational Physics, **73**, 2, 325–348, 1987, https://doi.org/10.1016/0021-9991(87)90140-9.

36. Y.J. LIU, *Fast Multipole Boundary Element Method Theory and Applications in Engineering*, Cambridge University Press, 2009, https://doi.org/10.1017/CBO9780511605345.

37. J. PTASZNY, M. HATŁAS, *Evaluation of the FMBEM efficiency in the analysis of porous structures*, Engineering Computations, **35**, 2, 843–866, 2018, https://doi.org/10.1108/EC-12-2016-0436.

38. L.H. DAI, Z.P. HUANG, R. WANG, *Explicit expressions for bounds for the effective moduli of multi-phased composites by the generalized self-consistent method*, Composites Science and Technology, **59**, 11, 1691–1699, 1999, https://doi.org/10.1016/S0266-3538(99)00031-7.

39. S. TORQUATO, *Random Heterogeneous Materials*, Springer-Verlag, New York, 2002, https://doi.org/10.1007/978-1-4757-6355-3.

40. A. GILLMAN, G. AMADIO, K. MATOUŠ, T.L. JACKSON, *Third-order thermo-mechanical properties for packs of platonic solids using statistical micromechanics*, Proceedings of The Royal Society A, 471, 20150060, 2015, https://doi.org/10.1098/rspa.2015.0060.

Received November 25, 2024; revised version March 17, 2025.
Published online June 16, 2025.